WATER RESOURCES RESEARCH, VOL. 30, NO. 6, PAGES 1665–1679, JUNE 1994

A distributed hydrology-vegetation model for complex terrain

Mark S. Wigmosta[1]
Department of Civil Engineering, University of Washington, Seattle

Lance W. Vail
Pacific Northwest Laboratory, Richland, Washington

Dennis P. Lettenmaier
Department of Civil Engineering, University of Washington, Seattle

Abstract. A distributed hydrology-vegetation model is described that includes canopy interception, evaporation, transpiration, and snow accumulation and melt, as well as runoff generation via the saturation excess mechanisms. Digital elevation data are used to model topographic controls on incoming solar radiation, air temperature, precipitation, and downslope water movement. Canopy evapotranspiration is represented via a two-layer Penman-Monteith formulation that incorporates local net solar radiation, surface meteorology, soil characteristics and moisture status, and species-dependent leaf area index and stomatal resistance. Snow accumulation and ablation are modeled using an energy balance approach that includes the effects of local topography and vegetation cover. Saturated subsurface flow is modeled using a quasi three-dimensional routing scheme. The model was applied at a 180-m scale to the Middle Fork Flathead River basin in northwestern Montana. This 2900-km^2, snowmelt-dominated watershed ranges in elevation from 900 to over 3000 m. The model was calibrated using 2 years of recorded precipitation and streamflow. The model was verified against 2 additional years of runoff and against advanced very high resolution radiometer based spatial snow cover data at the 1-km^2 scale. Simulated discharge showed acceptable agreement with observations. The simulated areal patterns of snow cover were in general agreement with the remote sensing observations, but were lagged slightly in time.

1. Introduction

Topography, soil characteristics, vegetation, and climate interact in a complex manner to determine the types, intensities, and locations of runoff production and the transport of sediments, chemicals, and organic debris in a landscape. Natural or human-induced changes to one or more of these forcing variables will alter the hydrologic response of a drainage basin. Prediction of the resulting changes in vegetation patterns, water quality, and runoff production requires an accurate, explicit representation of the relationships between hydrology, vegetation, and climate.

Hydrology and vegetation dynamics have, for the most part, been studied independently. Most vegetation models, for instance, the soil-vegetation-atmosphere schemes such as BATS [*Dickinson et al.*, 1986] and SiB [*Sellers et al.*, 1986], or the surface energy budget model of *Bonan* [1991] couple boundary layer micrometeorology theory with simplified resistance representations of plant physiology using a "flat Earth" approach. From a hydrological standpoint, a key assumption of these models is the absence of lateral redistribution of soil moisture. On the other hand, hydrologic models have mostly been concerned with runoff production; the representation of vegetation is often reduced to a specification of potential evapotranspiration and highly simplified soil moisture stress relationships.

Recently, attempts have been made to reconcile some of these differences. For instance, the Système Hydrologique Européen (SHE) [*Abbott et al.*, 1986a, b] simulates the complete hydrologic cycle, including a Penman-Monteith representation for evapotranspiration. *Famiglietti et al.* [1992] coupled TOPMODEL [*Beven and Kirkby*, 1979], as modified by *Sivapalan et al.* [1987], with a surface energy balance model to compute the spatial variability of evaporation at the catchment scale. *Running* [1991] and *Band et al.* [1991] have utilized geographic information processing, remote sensing, and the ecosystem model FOREST-BGC [*Running and Coughlan*, 1988] to simulate the patterns of forest evaporation. This work has been extended by *Band et al.* [1993], who coupled FOREST-BGC with TOPMODEL to account for the effects of lateral soil moisture redistribution on ecological processes.

Precipitation in mountainous regions contributes disproportionately to the surface hydrologic cycle of many areas of the globe. About 70% of the annual runoff in the western United States is derived from snowmelt in headwater catchments that compose less than 25% of the total land area [*Barros and Lettenmaier*, 1993]. In these regions, land surface characteristics such as topography, vegetation, and

[1]Now at Pacific Northwest Laboratory, Richland, Washington.

Copyright 1994 by the American Geophysical Union.

Paper number 94WR00436.
0043-1397/94/94WR-00436$05.00

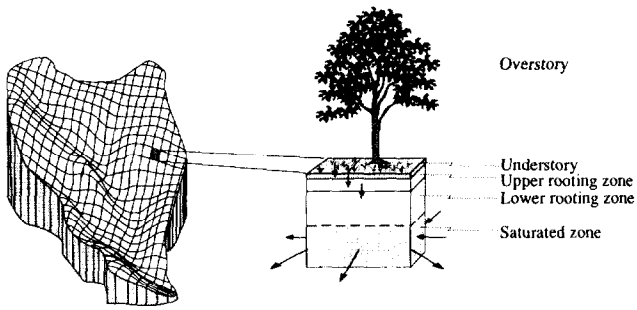

Figure 1. Model representation of a drainage basin. Digital elevation data are used to model topographic controls on incoming solar radiation, precipitation, air temperature, and downslope water movement. Linked one-dimensional moisture and energy balance equations are solved independently for each model grid cell. Grid cells are allowed to exchange saturated subsurface flow with their eight adjacent neighbors.

soils vary strongly in space. Meteorological forcings (precipitation, wind speed, etc.) exhibit similar spatial variation. The absorption of solar radiation is highly dependent on local topography. These small-scale heterogeneities impact soil moisture redistribution, runoff generation, and the land-surface energy balance. Statistical-dynamical methods like TOPMODEL maintain the spatial variability of a selected quantity (e.g., soil moisture), but information about the detailed location of heterogeneities is not retained. This information can be critical in evaluating the effects of natural phenomena such as climate change, or the impacts of human activities including deforestation, agriculture, and urbanization.

We describe here a physically based, distributed hydrology-vegetation model for complex terrain. The model accounts explicitly for the spatial distribution of land-surface processes, and can be applied over a range of scales, from plot to large watershed at subdaily to daily timescales. The level of model detail is sufficient to represent important processes and feedbacks within the hydrology-vegetation system in a physically realistic manner, consistent with the types of data likely to be available for model input and testing. Depending on the type, quality, and record lengths of site-specific data, the model can be run either using detailed field measurements, with parameter values taken from the literature, or using the output from other (e.g., orographic wind and precipitation) models.

2. Model Structure

The model structure is designed to provide an integrated representation of hydrology-vegetation dynamics at the topographic scale described by digital elevation data. It includes a two-layer canopy model for evapotranspiration, an energy balance model for snow accumulation and melt, a two-layer rooting zone model, and a saturated subsurface flow model. Digital elevation data are used to model topographic controls on incoming shortwave radiation, precipitation, air temperature, and downslope water movement. At each time step the model provides a simultaneous solution to the energy and water balance equations for every grid cell in the watershed. Individual grid cells are hydrologically linked through a quasi three-dimensional saturated subsurface transport scheme (Figure 1). A distinguishing feature of the model is that downslope redistribution of soil moisture via the saturated subsurface transport scheme is explicit; that is, accounting is done on a pixel-by-pixel basis, as contrasted with the statistical representation used, for instance, by TOPMODEL [*Beven and Kirkby*, 1979]. Computational efficiency of the subsurface model is attributable to the numerical scheme described by M. S. Wigmosta et al. (A simplified method for routing linked surface-subsurface flows in complex terrain, submitted to *Water Resources Research*, 1994; hereinafter Wigmosta et al. (submitted manuscript, 1994)).

Surface cover and soil properties are assigned to each digital elevation model (DEM) grid cell. These properties are allowed to vary spatially throughout the basin. In each grid cell the modeled land surface may be composed of overstory vegetation, understory vegetation, and soil. The overstory may cover all or a prescribed fraction of the land surface. The understory, if present, covers the entire ground surface. The model allows land surface representations ranging from a closed two-story forest, to sparse low-lying natural vegetation or crops, to bare soil.

The simulated soil/vegetation water balance for an individual grid cell (Figure 2) is written as

$$\Delta S_{s1} + \Delta S_{s2} + \Delta S_{io} + \Delta S_{iu} + \Delta W = P - E_{io} - E_{iu} - E_s - E_{to} - E_{tu} - P_2 \quad (1)$$

where ΔS_{s1} and ΔS_{s2} are the changes in upper and lower rooting zone soil water storage, respectively, ΔS_{io} and ΔS_{iu} are the changes in overstory and understory interception storages, respectively, ΔW is the change in snowpack water content, P is the volume of precipitation (rain and/or snow), P_2 is the discharge volume leaving the lower rooting zone, E_s is the volume of surface soil evaporation, and E_{io}, E_{iu}, E_{to}, and E_{tu} are the volumes of overstory and understory evaporation (from interception storage) and transpiration, respectively.

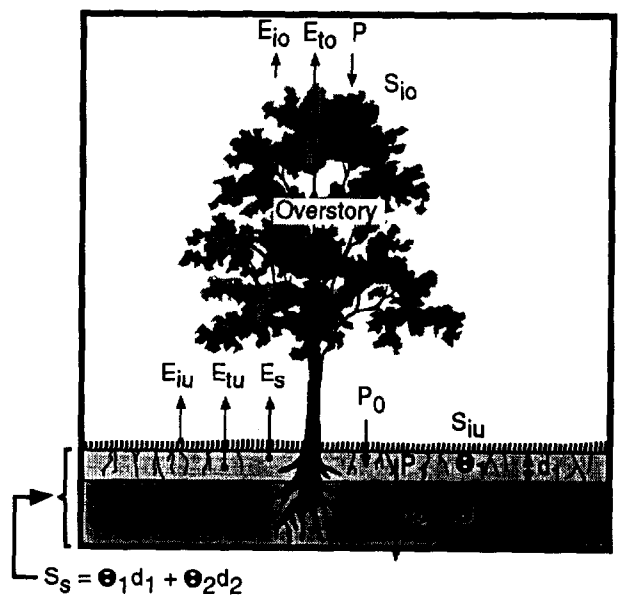

Figure 2. Simulated vegetation and rooting zone water balance for a model grid cell. Water leaving the lower rooting zone (P_2) recharges the local water table.

Local meteorological conditions (precipitation, air temperature, solar radiation, wind speed, and air vapor pressure) are prescribed for each grid cell at a specified distance above the overstory. Evapotranspiration from vegetation is modeled using a Penman-Monteith approach. The overstory is allowed to remove water from both the upper and lower soil zones, while the understory can only remove water from the upper zone. Solar radiation and wind speed are attenuated through the two canopies based on cover density and leaf area index (LAI), providing separate values for the overstory, understory, and soil. Stomatal resistance is calculated for each story based on local air temperature, the vapor pressure deficit, soil moisture conditions, and the photosynthetically active radiation flux. Soil water evaporation is dependent on the climatic demand, modulated by the soil's ability to supply water.

Snow accumulation and melt is simulated using a single-layer energy balance model that explicitly incorporates the effects of topography and vegetation cover on the energy exchange at the snow surface. Unsaturated moisture movement through the two rooting zone soil layers is calculated using Darcy's law. Discharge from the lower rooting zone recharges the local (grid cell) water table. Each grid cell exchanges saturated zone water with its eight adjacent neighbors as a function of water table depth, soil characteristics, and local topography, resulting in a transient, quasi three-dimensional representation of saturated subsurface flow. Return flow and saturation overland flow are generated in locations where grid cell water tables intersect the ground surface. The five submodels that describe the coupled moisture and energy balance, specifically evapotranspiration, shortwave and longwave radiation, snow accumulation and melt, unsaturated soil moisture, and saturated soil moisture are described in sections 2.1–2.5.

2.1. Evapotranspiration

Precipitation is assumed to be stored on the surfaces of overstory and understory vegetation until maximum interception storage capacities (I_{co} and I_{cu}) are reached. Any excess precipitation (throughfall) passes through the canopy with no attenuation. There is no distinction between rain and snow for interception storage. Maximum interception storage capacities (in meters) are determined from projected LAI [*Dickinson et al.*, 1991], with $I_{co} = 10^{-4}\ \mathrm{LAI}_o\ F$ and $I_{cu} = 10^{-4}\ \mathrm{LAI}_u$, where F is the fraction of ground surface covered by the overstory, and the subscripts o and u represent the overstory and understory, respectively. Changes in interception storage are given by

$$S_{ij}^{t+\Delta t} = S_{ij}^{t} + P - E_{ij} \tag{2}$$

where the subscript j denotes separate values for the overstory ($j = o$) and the understory ($j = u$). When $S_{ij}^{t+\Delta t}$ exceeds I_{cj}, throughfall is generated ($S_{ij}^{t+\Delta t} - I_{cj}$), and $S_{ij}^{t+\Delta t}$ is set equal to I_{cj}. P is equal to the overstory throughfall when (2) is applied to the understory.

Evaporation of intercepted water from the surfaces of wet vegetation is assumed to occur at the potential rate. Transpiration from dry vegetative surfaces is calculated using a Penman-Monteith approach

$$E_{tj} = \frac{\Delta R_{nj} + \rho c_p (e_s - e)/r_{aj}}{\lambda_v[\Delta + \gamma(1 + r_{cj}/r_{aj})]}\,\Delta t \tag{3}$$

where E_{tj} is the amount of water transpired over the time period Δt, Δ is the slope of the saturated vapor pressure–temperature curve, R_{nj} is the net radiation flux density, ρ is the density of moist air, c_p is the specific heat of air at constant pressure, e_s is the saturation vapor pressure, e is the vapor pressure, r_{aj} is the aerodynamic resistance to vapor transport, λ_v is the latent heat of vaporization of water, γ is the psychrometric constant, and r_{cj} is the canopy resistance to vapor transport. R_{nj}, r_{aj}, and r_{cj} are calculated separately for the overstory and understory (R_{no}, r_{ao}, r_{co} and R_{nu}, r_{au}, r_{cu}, respectively).

Evaporation from wet surfaces occurs at the potential rate which can be found by setting r_{cj} in (3) equal to zero

$$E_{pj} = \frac{\Delta R_{nj} + \rho c_p (e_s - e)/r_{aj}}{\lambda_v[\Delta + \gamma]}\,\Delta t \tag{4}$$

The ratio of transpiration from vegetation with a dry surface to the potential (wet surface) rate is given by dividing (3) by (4):

$$E_{tj}/E_{pj} = \frac{\Delta + \gamma}{\Delta + \gamma(1 + r_{cj}/r_{aj})} \tag{5}$$

The model calculates evaporation and transpiration independently for the overstory and understory in a stepwise fashion. First, intercepted water is evaporated at the potential rate

$$E_{ij} = \min\,(E_{pj},\ S_{ij}) \tag{6}$$

where E_{ij} is the amount of intercepted water evaporated over the time period and S_{ij} is the volume of intercepted water at the start of the time period. Transpiration from dry vegetation is then calculated using (4), (5), and (6):

$$E_{tj} = (E_{pj} - E_{ij})\,\frac{\Delta + \gamma}{\Delta + \gamma(1 + r_{cj}/r_{aj})} \tag{7}$$

This stepwise approach allows the vegetation surface to go from wet to dry during a time step (i.e., evaporation followed by transpiration). If the canopy remains completely wet or completely dry over the entire time step this method is equivalent to the direct application of the Penman-Monteith equation with the corresponding r_{cj}.

It is also possible to calculate evaporation from the soil using the Penman-Monteith equation with r_{cj} replaced by a soil surface resistance r_s [*Monteith*, 1981; *Shuttleworth and Wallace*, 1985; *Choudhury and Monteith*, 1988]. In most cases r_s is represented as an empirical function of near-surface soil moisture. However, we have chosen a less empirical soil physics–based approach to calculate soil evaporation [*Eagleson*, 1978a].

When wet, a soil may be able to supply water to the surface at a rate equal to or greater than the potential evaporation demand. This condition is termed climate-controlled [*Eagleson*, 1978b]. As soil moisture is depleted, the rate of delivery falls below the potential evaporation rate. At this and lower moisture states, the evaporation rate is termed soil-controlled and is a nonlinear function of the soil moisture content. Under this approach, soil water evaporation (E_s) is calculated as

$$E_s = \min\,(E_{ps},\ F_e) \tag{8}$$

where E_{ps} is calculated through (4) for conditions at the ground surface and F_e is the soil desorptivity, determined by the rate at which the soil can deliver water to the surface. Desorptivity is a function of soil type and moisture conditions in the upper soil zone and is discussed in section 2.4.2.

2.1.1. Aerodynamic resistance. Separate aerodynamic resistances are calculated for the overstory, understory, ground surface, and snow surface. With a complete overstory, the vertical wind velocity profile is modeled using three layers [*Campbell*, 1977]. A logarithmic wind speed profile is used above the overstory. Wind speed is assumed to decrease exponentially through the overstory and understory, merging into a new logarithmic profile near the ground or snow surface. Resistances to turbulent transport from the overstory, understory, and snow or soil are taken in series; thus

$$r_{au} = r_{\exp} + r_{ao} \tag{9}$$

$$r_{ag} \text{ (or } r_{as}) = r_{\log} + r_{\exp} + r_{ao} \tag{10}$$

where r_{ao}, r_{au}, r_{ag}, and r_{as} are the total aerodynamic resistances for the overstory, understory, ground, and snow, respectively. Resistance r_{ao} is associated with the upper logarithmic wind profile, $r_{\exp}$ with the exponential profile, and $r_{\log}$ with the lower logarithmic layer. These resistances vary with wind speed, overstory and understory height and LAI, snow or soil roughness, and atmospheric stability. Prognostic equations are developed in the appendix for each component in (9) and (10).

2.1.2. Canopy resistance. Canopy resistance (r_{cj}) is calculated separately for the overstory and understory ($j = o$ and $j = u$, respectively). For both stories r_{cj} is represented as a summation of the stomatal resistance, r_{sj} of individual leaves. The leaves are assumed to contribute in parallel so that

$$r_{cj} = \langle r_{sj} \rangle / c_j \mathrm{LAI}_j \tag{11}$$

where c_j is the appropriate ratio of total to projected LAI and the angle brackets denote an inverse average over the range of the canopy leaf area index [*Dickinson et al.*, 1991]. The dependence of r_{sj} on vegetation type and environmental factors is represented by a species-dependent minimum resistance (r_{smin_j}) and a product of four limiting factors each with a minimum value of one:

$$r_{sj} = r_{\mathrm{smin}_j} f_1(T_j) f_2(\mathrm{vpd}_j) f_3(\mathrm{PAR}_j) f_4(\theta_j) \tag{12}$$

where the environmental dependencies are f_1, air temperature (°C); f_2, vapor pressure deficit ($e_s - e$); f_3, photosynthetically active radiation flux (PAR); and f_4, soil moisture. Relations for the first three of these factors are taken from *Dickinson et al.* [1991] as

$$1/f_1 = 0.08T_a - 0.0016T_a^2 \tag{13}$$

$$1/f_2 = 1 - (e_s - e)/c_d \tag{14}$$

$$1/f_3 = \frac{r_{\mathrm{smin}}/r_{\mathrm{smax}} + R_p/R_{pc}}{1 + R_p/R_{pc}} \tag{15}$$

where T_a is the air temperature in degrees Celsius, c_d is the vapor pressure deficit causing stomatal closure (about 4 kPa), r_{smax} is the maximum (cuticular) resistance, R_p is the visible radiation, and R_{pc} is the light level where $r_s = 2r_{\mathrm{smin}}$.

Following *Feddes et al.* [1978] the model assumes a piecewise linear dependence of $1/f_4$ on soil moisture:

$$\begin{aligned} 1/f_4 &= 0 & \theta &\le \theta_{wp} \\ 1/f_4 &= \frac{\theta - \theta_{wp}}{\theta^* - \theta_{wp}} & \theta_{wp} &< \theta \le \theta^* \\ 1/f_4 &= 1 & \theta^* &< \theta \le \theta_s \end{aligned} \tag{16}$$

where θ is the average soil moisture content, θ_{wp} is the plant wilting point, and θ^* is the moisture content above which soil conditions do not restrict transpiration. For understory transpiration θ corresponding to the upper soil rooting zone is used. The overstory removes water from both rooting zones, and, as a result, separate calculations are made for each soil zone using the appropriate moisture content.

2.2. Shortwave and Longwave Radiation

2.2.1. Radiation budget without a snowpack. Separate shortwave and longwave radiation budgets are developed for the overstory, understory, and ground surface (Figure 3). The amount of shortwave radiation captured by the overstory is dependent on its projected LAI, fractional ground cover (F), reflectance coefficient (α_o), and transparency to shortwave radiation. Backreflection from the understory is also considered. The overstory shortwave radiation budget is given by

$$R_{so} = R_s[(1 - \alpha_o) - \tau_o(1 - \alpha_u)]F \tag{17}$$

where R_{so} is the shortwave radiation absorbed by the overstory, R_s is the incident shortwave radiation, α_u is the understory reflection coefficient, and τ_o is the fraction of shortwave radiation transmitted by the overstory canopy. The fraction of transmitted shortwave radiation is calculated following a Beer's law relationship of the form [*Monteith and Unsworth*, 1990]

$$\tau_o = \exp(-k\mathrm{LAI}_o) \tag{18}$$

where k is a canopy attenuation coefficient.

The understory receives attenuated shortwave radiation below the overstory ($R_s\tau_o F$) and direct shortwave radiation in the open ($R_s[1 - F]$). The total flux of shortwave radiation absorbed by the understory (R_{su}) is

$$R_{su} = R_s[[1 - \alpha_u] - \tau_u[1 - \alpha_g]][\tau_o F + [1 - F]] \tag{19}$$

where α_g is the soil reflection coefficient. The fraction of shortwave radiation transmitted by the understory (τ_u) is determined through (18) using the projected LAI of the understory vegetation (LAI_u). Shortwave radiation absorbed by the soil surface (R_{sg}) is given by

$$R_{sg} = R_s\tau_u(1 - \alpha_g)[[1 - F] + \tau_o F] \tag{20}$$

The overstory exchanges longwave radiation both with the sky and with the understory or soil:

$$R_{lo} = (L_d + L_u - 2L_o)F \tag{21}$$

where R_{lo} is the net overstory longwave radiation, and L_d, L_u, and L_o are downward sky, upward understory, and overstory longwave radiation fluxes, respectively. Assuming an emissivity of unity, $L_o = \sigma(T_o + 273)^4$ and $L_u = \sigma(T_u + 273)^4$, where σ is the Stefan-Boltzmann constant,

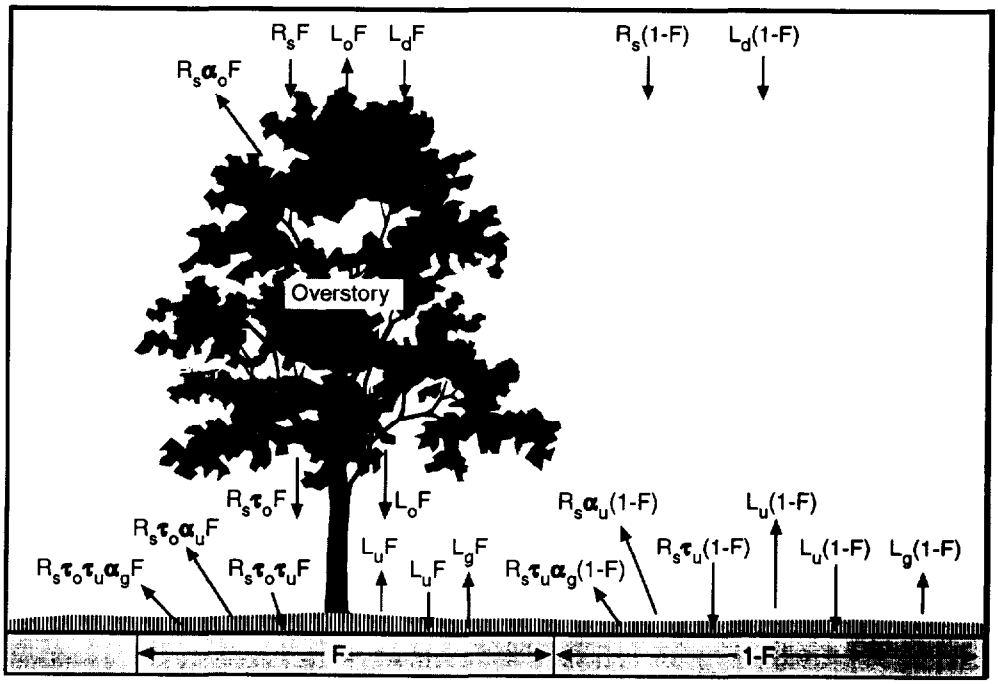

Figure 3. Shortwave and longwave radiation balance for a model grid cell without snow cover.

and T_o and T_u are the temperatures (degrees Celsius) of the overstory and understory, respectively. These two temperatures are set equal to the air temperature except when snow is on the ground (see section 2.2.2). Longwave radiation from the sky is supplied to the model.

Below the overstory, the understory exchanges longwave radiation with the overstory and the ground, while in the open it exchanges radiation with the sky and ground:

$$R_{lu} = \{[L_o + L_g - 2L_u]F\} + \{[L_d + L_g - 2L_u][1 - F]\} \quad (22)$$

where R_{lu} is the net understory longwave radiation, and L_g is the upward longwave flux from the soil calculated as $L_g = \sigma(T_g + 273)^4$ with T_g equal to the surface soil temperature. The surface soil temperature is normally taken equal to the air temperature except when snow is on the ground. This is done to avoid the necessity of an iterative solution to the nonlinear equation for surface temperature. We have, however, also implemented an iterative scheme that can be used when more accurate surface temperatures are required; the accuracy improvement is achieved at the expense of additional computational time, since the iteration must be performed at each grid cell.

2.2.2. Radiation budget with a snowpack. When a snowpack is present on a grid cell, it is assumed to either completely cover the overstory or remain entirely below the overstory, depending on the local vegetation height. The snowpack is always assumed to completely cover the understory and soil. As a result, the understory and soil do not contribute evapotranspiration (ET) and are ignored during ET calculations when a snowpack is present. In grid cells where the snowpack remains below the overstory, the snow reflectance coefficient (α_s) replaces α_o, α_u, and α_g in (17), (19), and (20). At the snow surface, (19) and (22) become

$$R_{ss} = R_s(1 - \alpha_s)\{\tau_o F + [1 - F]\} \quad (23)$$

$$R_{ls} = L_o F + \{L_d[1 - F]\} - L_s \quad (24)$$

where R_{ss} is the shortwave flux absorbed by the snow, R_{ls} is the net longwave exchange at the snow surface, and L_s is the upward longwave flux from the snow surface given by $L_s = \sigma(T_s + 273)^4$, with T_s equal to the temperature of the snow surface. On grid cells with snow over bare soil or over short vegetation, F in (23) and (24) is set equal to zero. The snow reflection coefficient is given by [*Laramie and Schaake*, 1972]

$$\alpha_s = 0.85(0.94)^{(N)^{0.58}} \quad (25a)$$

for the accumulation season, and

$$\alpha_s = 0.85(0.82)^{(N)^{0.46}} \quad (25b)$$

for the melt season, where N is the age of the snow surface in days since the last storm.

2.3. Snow Accumulation and Melt

Snow accumulation and melt are simulated using a single-layer, energy and mass balance model. The energy balance components are used to simulate snowmelt, refreezing, and changes in the snowpack heat content. The mass balance components represent snow accumulation/ablation, changes in snow water equivalent, and water yield from the snowpack.

2.3.1. Partition of precipitation. The partition of precipitation (P) into rain or snow is based on air temperature:

$$P_s = P \qquad T_a \le T_{\min}$$

$$P_s = \frac{T_{\max} - T_a}{T_{\max} - T_{\min}} \qquad T_{\min} < T_a < T_{\max} \tag{26a}$$

$$P_s = 0 \qquad T_a \ge T_{\max}$$

$$P_r = P - P_s \tag{26b}$$

where P_r and P_s are the water equivalent depths of rain and snow, respectively, $T_{\min}$ is a threshold temperature below which all precipitation is in the form of snow, and $T_{\max}$ is a threshold temperature above which all precipitation is rain. Between the threshold temperatures (typically, −1.1°C and 3.3°C) precipitation is assumed to be a mix of rain and snow. This is based on work by the *U.S. Army Corps of Engineers* [1956].

2.3.2. Snowpack energy balance. The snowpack energy balance is given by [*Anderson*, 1968]

$$c_s W \frac{dT_s}{dt} = R_{ns} + Q_s + Q_l + Q_p + Q_m + Q_g \tag{27}$$

where c_s is the specific heat of ice, W is the water equivalent of the snowpack, and t is time. The energy exchange at the snow-air interface is given by R_{ns}, the net radiation heat transfer adjusted for vegetative effects through (23) and (24); Q_s, the sensible heat transfer by turbulent convection; Q_l, the energy lost to evaporation and sublimation or the energy gained through the release of latent heat during condensation; and Q_p, the heat advected to the pack by rainfall. Q_m is the internal latent heat lost by melting, or heat gained by refreezing of liquid water. Fluxes into the pack are taken as positive. Heat transfer by conduction from the snow-ground interface (Q_g) is neglected.

The left-hand term in (27) is the change in snowpack cold content. The change in snowpack temperature at the end of the time step ($T_s^{t+\Delta t}$) is calculated through (27) as

$$T_s^{t+\Delta t} = T_s^t + \frac{\Delta t}{c_s W}\left[R_{ns} + Q_s + Q_l + Q_p + Q_m\right] \tag{28}$$

with $T_s \le 0$. When T_s remains below 0°C over the time step, Q_m represents the gain (positive flux) of internal latent heat from refreezing of liquid water in the snowpack. During periods of melt the pack is isothermal at 0°C (i.e., $T_s^{t+\Delta t} = 0$), allowing the heat flux available for snowmelt to be calculated from (28) as

$$Q_m = R_{ns} + Q_s + Q_l + Q_p + c_s W T_s^t \tag{29}$$

The sensible heat transfer is given by

$$Q_s = \frac{\rho c_p (T_a - T_s)}{r_{as}} \tag{30}$$

where r_{as} is adjusted for the effects of vegetation and atmospheric stability. The latent heat transfer is taken equal to

$$Q_e = \frac{\lambda_i \rho \left[\dfrac{0.622}{P_a}\right]\left[e(T_a) - e_s(T_s)\right]}{r_{as}} \tag{31}$$

where P_a is the atmospheric pressure, and λ_i equals the latent heat of vaporization during periods of melt (evaporation/condensation) and λ_i equals the latent heat of fusion during nonmelt periods (sublimation).

The energy advected by precipitation is

$$Q_p = \rho_w c_w T_p (P_r + 0.5 P_s) \tag{32}$$

where c_w is the specific heat of water and T_p is the temperature of the precipitation (taken equal to the air temperature). The specific heat of ice is one-half that of water, which accounts for the term $0.5P_s$.

Latent heat transfer from melting or refreezing is calculated by

$$Q_m = \lambda_f \rho_w M \tag{33}$$

where M is the depth of snowmelt (negative flux) or the volume of liquid water refrozen (positive flux).

2.3.3. Snowpack mass balance. The snowpack is composed of two phases, water and ice:

$$W = W_{\text{liq}} + W_{\text{ice}} \tag{34}$$

where W_{liq} is the volume per unit area (depth) of liquid water and W_{ice} is the water equivalent of ice. Mass balance for each phase is given by

$$\Delta W_{\text{liq}} = \left[P_r + \frac{Q_e}{\rho_w \lambda_v} - \frac{Q_m}{\rho_w \lambda_v}\right]\Delta t \tag{35}$$

$$\Delta W_{\text{ice}} = \left[P_s + \frac{Q_e}{\rho_w \lambda_f} + \frac{Q_m}{\rho_w \lambda_f}\right]\Delta t \tag{36}$$

During nonmelt periods the atmosphere exchanges water vapor with the ice phase, while during active melt the atmosphere exchanges water with the liquid phase. This is equivalent to setting $Q_e = 0$ in (35) when $T_s < 0$°C and setting $Q_e = 0$ in (36) when $T_s = 0$°C. A positive Q_e adds mass to the snowpack.

During melt, Q_m is negative, removing mass from the ice phase and increasing the liquid phase. Water is removed from the pack when the liquid phase exceeds the current liquid water storage capacity of the snowpack (taken equal to $0.06W$):

$$M_p = W_{\text{liq}}^{t+\Delta t} - 0.06 W^{t+\Delta t} \qquad M_p > 0 \tag{37}$$

where M_p is the depth of meltwater removed from the pack per unit area.

2.4. Unsaturated Soil Moisture Movement

The model does not have an infiltration equation; all throughfall or snowmelt enters the soil column. If the soil becomes saturated the excess water becomes surface runoff. The dynamics of unsaturated moisture movement are simulated using a two-layer model. The thickness of the upper zone (d_1) is equal to the average rooting depth of the understory vegetation (Figure 2). The lower zone extends from d_1 to the average overstory rooting depth. The understory can only extract water from the upper zone, while the overstory can remove water from both zones. Overstory transpiration from each soil zone is calculated using (7), then multiplied by the overstory root fraction in that zone. Soil evaporation is restricted to the upper zone.

The mass balance for the upper and lower zones is given by

$$d_1(\theta_1^{t+\Delta t} - \theta_1^t) = P_0 - P_1(\theta_1) - E_{to} - E_{tu} - E_s + V_{sat} - V_r \quad (38)$$

$$d_2(\theta_2^{t+\Delta t} - \theta_2^t) = P_1(\theta_1) - P_2(\theta_2) - E_{to} + V_{sat} \quad (39)$$

where d_2 is the lower zone thickness, θ_j is the average soil moisture, P_0 is the volume of infiltrated rainfall or snowmelt, E_s is the volume of evaporated soil moisture, V_{sat} is the volume of water supplied by a rising water table, V_r is the volume of return flow (generated when a rising water table reaches the ground surface), and P_1 and P_2 are downward volumes of water discharged from the upper and lower soil zones over the time step, respectively.

2.4.1. Percolation. The discharge volumes P_1 and P_2 are based on average soil moisture conditions during the time step, Δt. Discharge is calculated via Darcy's law assuming a unit hydraulic gradient:

$$P_j = K_v(\theta_j) \quad (40)$$

where $K_v(\theta_j)$ is the soil vertical unsaturated hydraulic conductivity and j equals 1 for the upper layer and 2 for the lower layer. The Brooks-Corey [*Brooks and Corey*, 1964] equation is used to calculate hydraulic conductivity:

$$K_v(\theta) = K_v(\theta_s)\left[\frac{\theta - \theta_r}{\phi - \theta_r}\right]^{(2/m)+3} \quad (41)$$

where m is the pore size distribution index, ϕ is the soil porosity, and θ_r is the residual soil moisture content. For simplicity, the saturated moisture content θ_s is taken equal to ϕ (i.e., $\theta_r = 0$).

The discharge volume over the time step is given as

$$P_j = \left[\frac{K_v(\theta_j^t) + K_v(\theta_j^*)}{2}\right]\Delta t \quad (42)$$

where $\theta_j^* = \theta_j^t + (P_{j-1}/d_j)$.

2.4.2. Desorption. Soil water evaporation from the upper soil layer E_s is given by (8) as a function of the potential evaporation demand at the soil surface (E_{ps}) and F_e, the desorption volume. *Eagleson* [1978a] provides an approximate solution for the rate at which a uniformly wetted, semi-infinite porous medium loses moisture to vertical (upward) desorption:

$$f_e = \tfrac{1}{2} S_e t^{-1/2} - \frac{K(\theta^{z,0}) + K(\theta^{0,t})}{2} \quad (43)$$

where S_e is termed the soil sorptivity. The second term on the right-hand side of (43) accounts for the influence of gravity. The effects of this term will be approximated by (42). Thus (43) is replaced by

$$f_e = \tfrac{1}{2} S_e t^{-1/2} \quad (44)$$

Following the approach of *Entekhabi and Eagleson* [1989], at the beginning of a time step the soil moisture content is assumed to be uniform (i.e., unit gradient assumption), and t in (44) is reset to zero. The depth of the upper layer must be larger than the depth of moisture extraction during the time step for this semi-infinite initial condition to be valid.

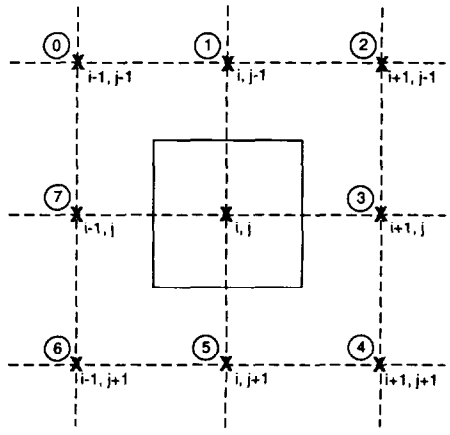

Figure 4. Schematic of solution grid for subsurface flow routing. Grid cells are centered around each DEM elevation point (solid square surrounding the node i, j). Directions relative to each elevation point are designated by the index k and numbered from 0 to 7 in a clockwise manner starting with the upper left-hand node.

The desorption volume (F_e) is obtained by integrating (44) over the time step

$$F_e = \int_{t=0}^{t=\Delta t} \frac{1}{2} S_e t^{-1/2}\, dt = S_e \Delta t^{1/2} \quad (45)$$

Sorptivity is calculated using the method presented by *Entekhabi and Eagleson* [1989]:

$$S_e = \left[\frac{8\phi K(\theta_s)\psi_b}{3(1+3m)(1+4m)}\right]^{1/2}\left[\frac{\theta}{\phi}\right]^{(1/2m)+2} \quad (46)$$

where ψ_b is the soil bubbling pressure.

2.5. Saturated Subsurface Flow

The quasi three-dimensional saturated subsurface flow model of Wigmosta et al. (submitted manuscript, 1994) is used. Only an outline of the method is presented here. The reader is referred to Wigmosta et al. (submitted manuscript, 1994) for details. The effects of topography on flow routing are obtained through the direct use of DEM data. Each grid cell can exchange water with its eight adjacent neighbors (Figure 4). Local hydraulic gradients are approximated by local ground surface slopes (kinematic approximation). Thus a given grid cell will receive water from its upslope neighbors and discharge to its downslope neighbors. In each cell, transient conditions are approximated by a series of steady state solutions based on local hydraulic conditions.

Grid cells are centered at each elevation point (e.g., solid square surrounding the elevation point i, j in Figure 4). Directions between a node and its eight adjacent neighbors are assigned the index k and numbered from 0 to 7 in a clockwise direction. For example, $k = 2$ corresponds to the direction between elevation point i, j and point $i + 1, j - 1$. The rate of saturated subsurface flow at time t from cell i, j to its downgradient neighbors is equal to

$$q(t)_{i,j,k} = T(t)_{i,j}\beta_{i,j,k}w_k \qquad \beta_{i,j,k} < 0$$
$$q(t)_{i,j,k} = 0 \qquad \beta_{i,j,k} \geq 0 \quad (47)$$

where $q_{i,j,k}$ is the flow rate from cell i, j in the k flow direction, $T_{i,j}$ is the transmissivity at cell i, j, $\beta_{i,j,k}$ is the ground surface slope in the k direction, and w_k is the width of flow in the k direction. Flows leaving a cell are negative ($\beta_{i,j,k} < 0$).

Beven [1982] has provided evidence suggesting that saturated hydraulic conductivities for some soils decrease with depth below the soil surface in a manner that can be approximated by a simple exponential function. This allows soil transmissivity in (47) to be calculated as

$$T_{i,j} = [Ks_{i,j}[\exp(-f_{i,j}z_{i,j}) - \exp(-f_{i,j}D_{i,j})]][f_{i,j}]^{-1} \quad (48)$$

where $Ks_{i,j}$ is the lateral component of soil saturated hydraulic conductivity for cell i, j, $z_{i,j}$ is the distance from the ground surface to the water table (positive downward), $f_{i,j}$ is a parameter related to the decay of saturated conductivity with depth, and $D_{i,j}$ is the total soil depth. Substituting (48) into (47) yields

$$q(t)_{i,j,k} = \gamma_{i,j,k}h_{i,j}(t) \quad (49)$$

where

$$\begin{aligned} \gamma_{i,j,k} &= w_k Ks_{i,j}\beta_{i,j,k}/f_{i,j} \qquad \beta_{i,j,k} < 0 \\ \gamma_{i,j,k} &= 0 \qquad\qquad\qquad\qquad \beta_{i,j,k} \geq 0 \end{aligned} \quad (50)$$

$$h_{i,j}(t) = \exp(-f_{i,j}z_{i,j}(t)) - \exp(-f_{i,j}D_{i,j}) \quad (51)$$

The time-invariant values for $\gamma_{i,j,k}$ are only calculated once, at the start of a model run.

The total saturated subsurface outflow from cell i, j($Q_{\text{out}_{i,j}}$) is calculated as

$$Q_{\text{out}_{i,j}} = h_{i,j}(t)\sum_{k=0}^{7}\gamma_{i,j,k} \quad (52)$$

The total inflow to cell i, j from upslope cells ($Q_{\text{in}_{i,j}}$) is given by

$$Q_{\text{in}_{i,j}} = h_k(t)\sum_{k=0}^{7}\gamma_k \quad (53)$$

where in this case k represents the source grid cell location. For example, $k = 4$ specifies inflow from cell $i + 1$, $j + 1$ with Q_{out_k} calculated using $h_k = \exp(-f_{i+1,j+1}z_{i+1,j+1}) - \exp(-f_{i+1,j+1}D_{i+1,j+1})$.

The mass balance for cell i, j is

$$\Delta S_{\text{sat}_{i,j}} = [P_{2_{i,j}}A_{i,j} + Q_{\text{in}_{i,j}} + Q_{\text{out}_{i,j}}]\Delta t \quad (54)$$

where $\Delta S_{\text{sat}_{i,j}}$ is the change in the saturated volume of water over the time period Δt, $P_{2_{i,j}}$ is the input of discharge from the unsaturated zone given by (42), $A_{i,j}$ is the cell area (horizontal projection), and $Q_{\text{out}_{i,j}}$ is negative via (50). Changes in depth to the water table are calculated as

$$z_{i,j}^{t+\Delta t} = z_{i,j}^{t} - \frac{\Delta_{\text{sat}_{i,j}}}{A_{i,j}(\theta_{s_{i,j}} - \theta_{i,j})} \quad (55)$$

where $\theta_{s_{i,j}}$ is the saturated soil moisture content and $\theta_{i,j}$ is the current average moisture content above the water table calculated through (38) or (39) depending on the location of the water table.

Negative values of $z_{i,j}$ represent "exfiltration" of subsurface water to the surface, with the volume (V_r) given by $V_r = -z_{i,j}^{t+\Delta t}(\theta_{s_{i,j}} - \theta_{i,j})A_{i,j}$. Exfiltration is most common is depressions, valley bottoms, and areas of topographic convergence. No channel system is imposed on the DEM (or model); it is formed and maintained entirely through the downslope redistribution of soil water. Subsurface water is exfiltrated within the drainage network and is assumed to exit the basin the same day it is generated.

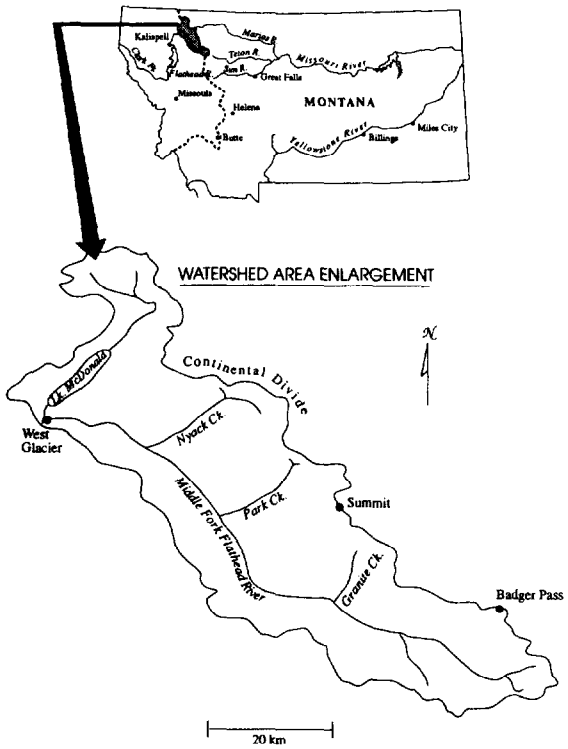

Figure 5. Middle Fork Flathead catchment location map.

3. Test Application

The model was applied to the Middle Fork Flathead River basin located in northwestern Montana (Figure 5). This 2900-km^2 catchment ranges in elevation from 960 m at the outlet (114°00'33"W, 48°29'43"N) to over 3000 m along the Continental Divide, which forms its eastern boundary. Precipitation increases with elevation, with measured values of 745 mm/yr at West Glacier (elevation 960 m) and 1387 mm/yr at the Soil Conservation Service (SCS) Badger Pass Snotel site (2100 m in elevation). About two thirds of the precipitation falls between October and April. At West Glacier, average monthly minimum air temperature remains below freezing from October to April, reaching a low of −10°C in January. Average monthly maximum temperatures are below 0°C in December and January, with a high of 26°C in July. Mean annual flow at the outlet is 2.4 mm/d, ranging from 0.6 mm/d in February to 8.6 mm/d in June. Runoff is snowmelt-dominated, with 78% of the yearly discharge volume occurring between April and July; May and June account for 58% of the yearly total.

3.1. Implementation

The model was run at a 3-hour time step over a DEM with 180-m grid spacing. Daily values of precipitation and maxi-

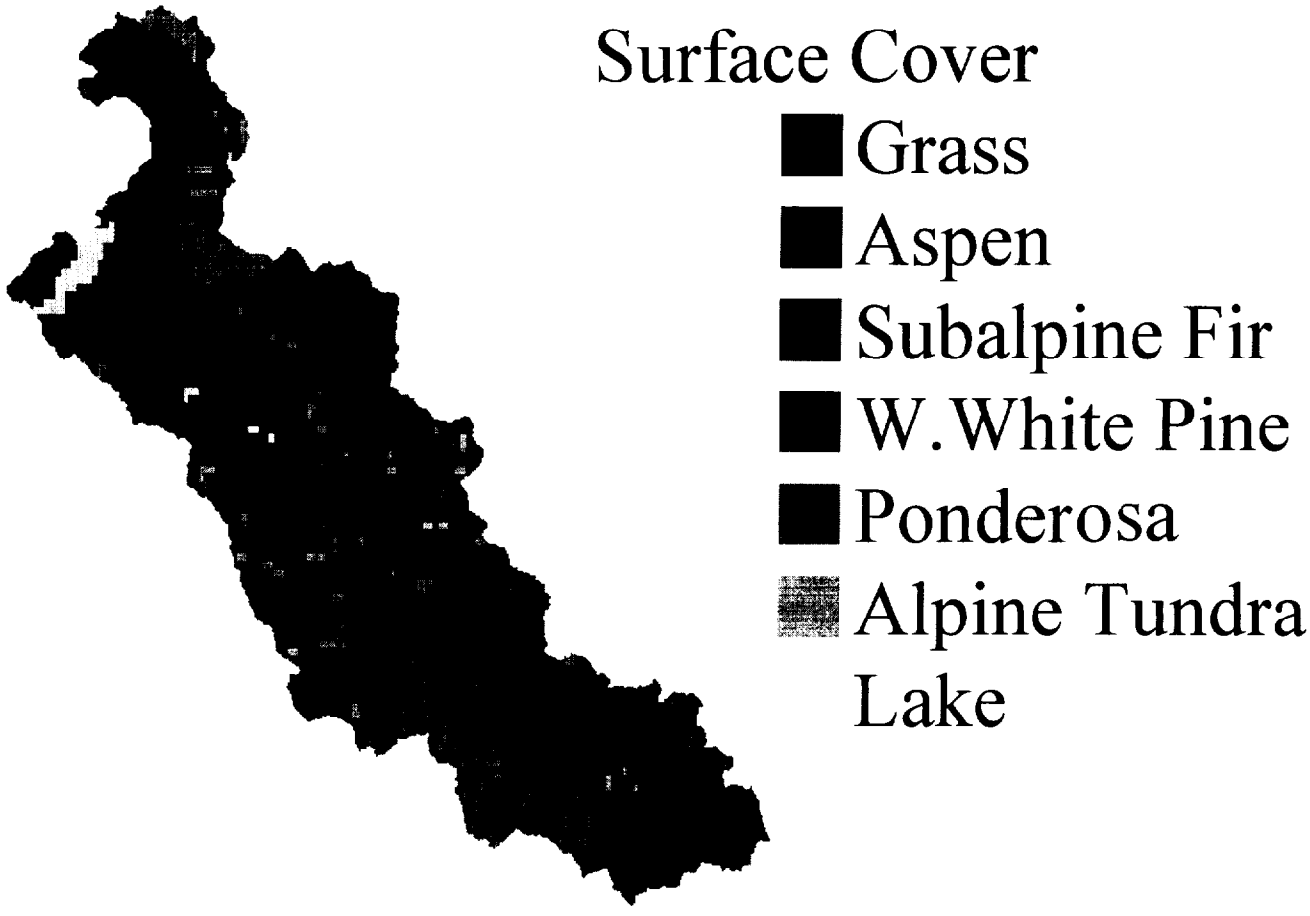

Figure 6. Distribution of surface cover estimated from normalized difference vegetation index data.

mum and minimum air temperature were available from weather stations located near the outlet (West Glacier) and at Badger Pass. Precipitation was distributed uniformly over the day and scaled for elevation using a linear relation between daily totals at the two weather stations. Daylight air temperature was modeled using three quadrants of a sine wave ($-\pi/2$ to π) with the minimum value at sunrise and the maximum value at two thirds of the day length ($\pi/2$). A linear change in air temperature was used during the night. The diurnal air temperature trace was calculated from measurements at West Glacier and corrected for elevation using a lapse rate of 6°C/km. Air vapor pressure was estimated from minimum air temperature at West Glacier and was corrected for elevation via the method of *Running et al.* [1987]. Wind speed data were not available within the basin; therefore a constant value of 2 m/s was used for all grid cells.

Clear-sky solar radiation was calculated for each grid cell prior to the model run using the Image Processing Workbench [*Frew*, 1990; *Longley*, 1992]. These algorithms account for the date, time of day, grid cell location, slope, and aspect, and the effects of shading or reflection of shortwave radiation from surrounding terrain. For each month, the day whose calculated clear-sky shortwave radiation is closest to the monthly average (based on a horizontal surface) was used to compute solar radiation during the month. These 12 days were broken into 3-hour intervals. For each interval, the time whose instantaneous radiation equals the interval average was used to calculate separate values of direct beam and diffuse radiation for each grid cell. Following the method of *Arola* [1993], these values were separated into 10 classes (with nearly equal numbers of members) for each component. Thus each grid cell was assigned a class for direct beam and diffuse radiation for each time step. The grid cell classifications and corresponding radiation values were read from disk for each month during the model run. These values were corrected for daily atmospheric transmittance, which was estimated from the daily range in air temperature at West Glacier using the method of *Bristow and Campbell* [1984]. The classification scheme used produces sufficient spatial resolution for modeling purposes.

The spatial distribution of vegetation was estimated using a vegetation classification for the continental United States at a resolution of 30 arc sec (approximately 1 km) produced by the Environmental Research Laboratory, U.S. Environmental Protection Agency, Corvallis, Oregon [*Loveland et al.*, 1991]. Each grid cell was assigned one of the following cover types: no cover (lakes), grass, Aspen, subalpine fir, or pine (western white, ponderosa, and lodgepole) (Figure 6). The values for vegetation parameters used in the simulation are presented in Table 1. Separate values of LAI were used for the summer (May to September) and winter months. The estimated LAI was interpolated to the 180-m scale using a nearest neighbor approach.

There are insufficient data to map the spatial distribution

Table 1. Vegetation Parameter Values Used in Middle Fork Flathead Simulations

Parameter	Grass	Aspen	Subalpine Fir	Pine
Summer LAI, m^2/m^2	1.3	4.0	4.0	3.0
Winter LAI, m^2/m^2	1.3	0.5	4.0	3.0
α	0.18	0.18	0.18	0.18
R_{smin}, s/cm	1.2	5.0	25.0	8.0
R_{smax}, s/cm	50.0	50.0	50.0	50.0
R_{cp}, W/m^2	30.0	30.0	30.0	30.0

Summer LAI data from *Kaufmann et al.* [1982]; R_{smin} data from *Kaufmann* [1982]; *Alexander et al.* [1985], and *Hunt et al.* [1991]; R_{smax} data from *Dickenson et al.* [1986]; R_{cp} data from *Dickenson et al.* [1991].

of soil properties. The basin is composed largely of silt loams. A vertical saturated conductivity of 0.013 m/h, a saturated moisture content of 0.49, and a field capacity of 0.33 were used in all grid cells. These are representative laboratory values for silt loam [*Rawls and Brakensiek*, 1989].

3.2. Simulation Results

The model was calibrated to discharge at the gage near West Glacier in water years 1988 and 1989, and was verified using discharge and spatial snow cover data from 1990 and 1991. We chose not to adjust vegetation parameters or soil hydraulic properties except Ks and f. The model was first calibrated to annual discharge by multiplying elevation-corrected precipitation by 1.16, which resulted in a total simulated flow volume within 1.1% of recorded. This gage correction is at the lower end of reported gage catch deficiencies [*Linsley et al.*, 1982]. *Legates and DeLiberty* [1993] found undercatch biases in gage measured winter precipitation can exceed 20% in northwestern Montana.

The model was then calibrated to daily streamflow by adjusting soil thickness, rooting zone thickness, and lateral saturated hydraulic conductivity within "reasonable" ranges, resulting in final values for all grid cells of $d_1 = d_2 = 0.2$ m, $D = 1.5$ m, $K_s = 1.0$ m/h, and $f = 0.2$ (Figure 7). Daily simulated flows have a root-mean square error (RMSE) of 1.2 mm and correlation coefficient (R^2) of 0.95 with the observations. The model tends to slightly oversimulate hydrograph recession associated with spring and summer melt during the calibration period and undersimulate low flow during the winter accumulation season. The model was verified using the next 2 years of data (Figure 7). The daily simulation RMSE during the verification period was 2.3 mm with an R^2 of 0.91. Total flow volume is undersimulated by 7%.

The snow accumulation and melt module was tested as a point model without calibration using daily SCS Snotel data from Badger Pass for water years 1989–1992 (Figure 8). Simulated snow water equivalent shows good agreement with recorded in the accumulation season. The model has a small bias toward simulating snowmelt too early.

The model's representation of spatial snowpack dynamics was assessed by comparing the areal extent of simulated snow cover with snow cover patterns obtained from advanced very high resolution radiometer (AVHRR) data during the melt seasons of 1990 and 1991. The AVHRR data are available from the National Operational Hydrologic Remote Sensing Center (Minneapolis, Minnesota) at approximately 2-week intervals beginning in 1990; however, cloud cover reduces the number of usable images. Due to the short length of this record, we were not able to calibrate the model to snow area extent using these data. However, the AVHRR data were available for the model verification years. Four days with minimal cloud cover during the ablation season were selected for comparison: May 10, 1990, and June 21, 1990, and April 22, 1991, and June 2, 1991. On May 10, 1990, recorded snow-free areas are restricted to lower elevations near the outlet and the lower valley of the Middle Fork Flathead River (Figure 9). Simulated snow-free areas are less broad and more confined to low-elevation valleys. Over one half of the basin is snow-free by June 21, 1990. Simulated snowpack removal lags recorded for this date. However, the pattern of snow-free areas is in general agreement with recorded. Simulated snow removal is greater on southern facing slopes due to increased solar radiation (this is particularly true in the main tributary valleys). The poorest model performance is evident on April 22, 1991, where the

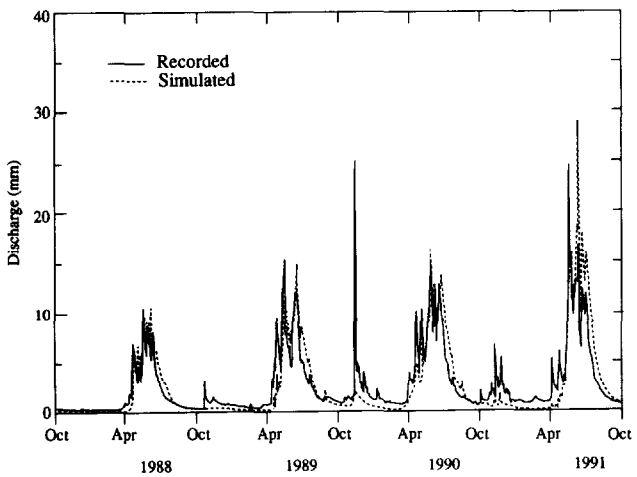

Figure 7. Simulated and recorded streamflow for 1988–1991. The model was calibrated to data from 1988 and 1989 and was verified against discharge from 1990 and 1991.

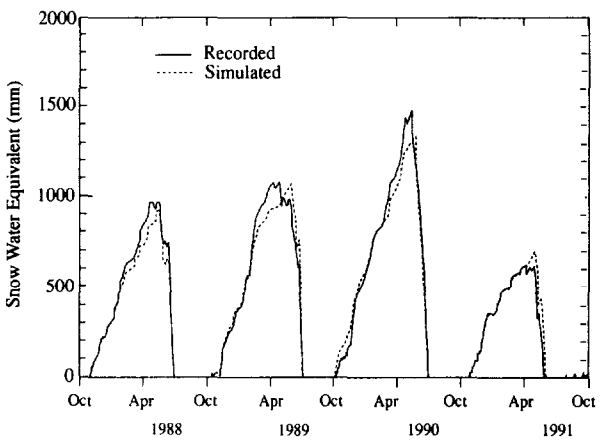

Figure 8. Simulated and recorded snow water equivalent based on daily Soil Conservation Service Snotel data from Badger Pass for 1989–1992.

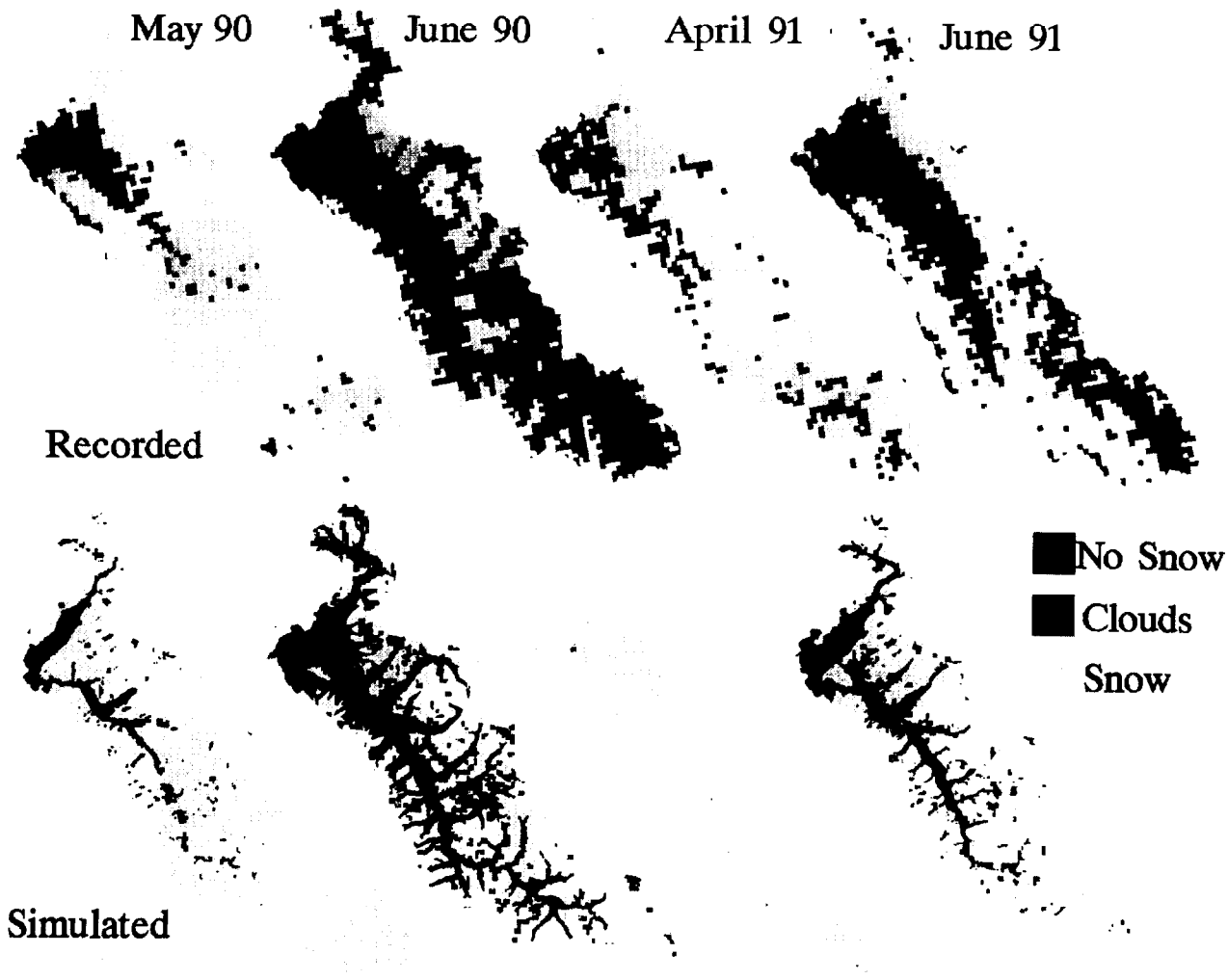

Figure 9. Areal extent of recorded snow cover based on AVHRR data (first row) and simulated snow cover (second row) for May 10, 1990, June 21, 1990, April 22, 1991, and June 2, 1991.

model substantially overpredicts the areal extent of snow cover. Simulation results are improved in the June 2 simulation, although the model still underpredicts the extent of snow-free areas, particularly in the southeastern portion of the basin.

The simulated patterns of snow cover are in general agreement with recorded, but are lagged in time. Much of this discrepancy may result from an incorrect spatial representation of meteorological parameters, especially precipitation where spatial observations are not available. A comparison of AVHRR data for June 21, 1990, and June 2, 1991, (Figure 9) shows substantially different patterns of snow cover, implying different snow accumulation patterns from those simulated with the simple precipitation lapsing we used. We also believe that the AVHRR estimate of snow areal extent may miss some snow cover below the forest canopy and therefore tend to underestimate snow areal extent.

The modeled areal extent of snow cover (Figure 10, first row) and snowmelt influences strongly the spatial patterns of simulated soil moisture (Figure 10, second row). In the spring and early summer, regions of surface saturation coincide with stream valleys and areas of recent or active melt. On May 10, surface saturation is restricted to Lake McDonald and lower elevation valleys. The "ring" of high soil moisture around Lake McDonald (near the basin outlet) and at the base of the wide valley bottoms results from the DEM resolution and the kinematic subsurface routing scheme used. These areas appear essentially flat at the DEM resolution. Saturated subsurface flow tends to accumulate at the first apparently flat pixel. We are presently testing a Dupuit routing scheme which we believe will correct this problem.

By June 21, the higher elevations show increased soil moisture resulting from active snowmelt (Figure 10). In July, middle- and lower-elevation slopes have began to dry, and greater soil moisture remains widespread at higher elevations. By mid-August, only the highest elevations with the most recent snowmelt retain high levels of soil moisture. Throughout the remainder of the summer and early fall the entire basin dries, and higher values of soil moisture are restricted to Lake McDonald, the major valleys, and local zones of convergent topography or depressions. This pattern is essentially retained until soil moisture is recharged in the following spring melt.

Evapotranspiration (ET) follows a pattern that is linked

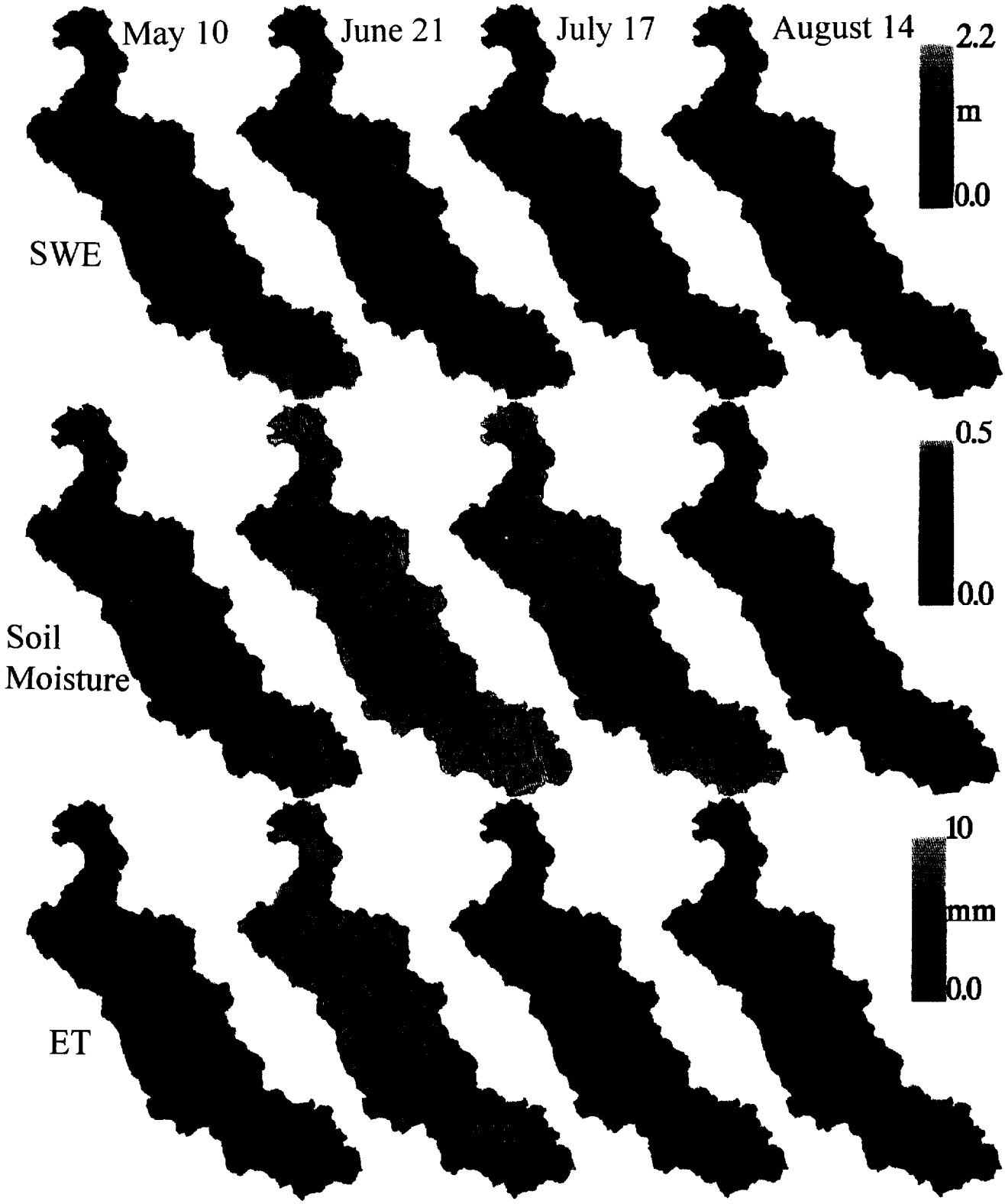

Figure 10. Simulated snow water equivalent (SWE, first row), upper rooting zone volumetric soil moisture (second row), and daily evapotranspiration (ET, third row) for May 10, June 21, July 17, and August 14, 1990. A volumetric soil moisture of 0.5 corresponds to saturation.

strongly to soil water and weather conditions (Figure 10, third row). In the spring, ET is the highest in the lower-elevation valleys where soil moisture and air temperature are the greatest. The magnitude of evapotranspiration increases in June and early July, resulting from relatively high soil moisture and greater air temperature and incoming solar radiation. By mid-July, evapotranspiration is greatest at the higher elevations due to the relatively higher soil moisture there. Evapotranspiration decreases rapidly in the fall due to low soil moisture, and reduced solar radiation and air temperature.

4. Summary and Conclusions

We have described a spatially distributed hydrology-vegetation model that includes canopy interception, evaporation, transpiration, and snow accumulation and melt, as well as saturation excess runoff generation. Digital elevation data are used to model important topographic controls on incoming solar radiation and downslope water movement. The model is capable of performing multiple-year simulations at spatial resolutions resulting in $O(10^5)$ pixels on medium-range RISC workstations (e.g., Sun Sparc 10). The model was applied to the 2900-km^2, snowmelt-dominated Middle Fork Flathead River basin, located in northwestern Montana. Simulated discharge showed acceptable agreement with recorded over the 4-year calibration and verification period. We attempted to validate the model's spatial representation of snowpack dynamics by comparing simulated snow cover with AVHRR data. The simulation results were in general agreement with those obtained with AVHRR data, although they were lagged in time slightly.

As with all models of this type, the availability of spatially distributed data for model input and verification is limited, particularly in mountainous regions. Our snow cover simulations, in particular, indicate that improved model performance will require a more accurate representation of orographic affects on wind speed, precipitation, and air temperature. In this respect, recent progress in orographic precipitation modeling is promising, and we expect that in the near future it will be possible to couple orographic precipitation and wind models with the vegetation-hydrology model described herein. Nonetheless, the availability of distributed surface energy and moisture flux data, which to date have only been collected at a few small catchments (e.g., First International Satellite Land Surface Climatology Project (ISLSCP) Field Experiment (FIFE) [*Sellers et al.*, 1992]), none of which are in mountainous environments, will ultimately be needed to fully assess the accuracy of the model.

Appendix: Aerodynamic Resistance Formulation

The aerodynamic resistance to heat and water vapor transfer in (9) and (10) is assumed equal to the momentum resistance. Following *Shuttleworth and Wallace* [1985], these resistances are assumed to vary linearly with overstory density. The effective sources for the overstory and understory are taken at heights $(d_j + z_{0j})$ where d_j is the zero-plane displacement, z_{0j} is the roughness length, and j equals u for the understory and o for the overstory. Under fully developed conditions these terms are taken as $d_j = 0.63h_j$ and $z_{0j} = 0.13h_j$, where h_j is the average vegetation height. The upper limit of the lower logarithmic velocity profile (height z_n) is taken equal to one tenth of the understory height or one tenth of the overstory height if no understory is present.

In neutral conditions the aerodynamic resistance for momentum transfer with a logarithmic profile is given by

$$r_{\log} = \frac{\ln (Z'/Z'')^2}{u(r)k^2} \tag{A1}$$

where k is von Karman's constant (taken as 0.41), $u(r)$ is the wind speed at the reference height r, and the two Z terms are a function of surface conditions. The aerodynamic resistance between the atmosphere and the overstory (r_{ao}) is calculated from (A1) with $Z' = x - d_o$, $Z'' = z_{0o}$, and $r = x$ (the measurement height). The resistance $r_{\log}$ in (10) is given by (A1) with $Z' = z_n$, $r = z_n$, and Z'' equal to the surface roughness for soil (z_{0g}) or to the snow depth and roughness ($z_s + z_{0s}$) if a snowpack is present below the overstory.

At the top of the overstory the eddy diffusion coefficient in the exponential layer (K_e) equals the logarithmic diffusion coefficient (K_l)

$$K_e = K_l(h_o) \exp [n[z/h_o - 1]] \tag{A2}$$

where

$$K_l(h_o) = \frac{u(x)k^2(h_o - d_o)}{\ln [[x - d_o]/z_{0o}]} \tag{A3}$$

and n is an extinction coefficient, with a typical value of 2–3. The resistance $r_{\exp}$ is given by

$$r_{\exp} = \int_{Z'''}^{d_o + z_{0o}} \frac{1}{K_e}\, dz = \frac{h_o e^n}{nK_l(h_o)} [\exp (-nZ'''/h_o) - \exp [-n[d_o + z_{0o}]/h_o]] \tag{A4}$$

where $Z''' = d_u + z_{0u}$ in (9) and $Z''' = z_n$ in (10).

A1. Resistances With No Overstory

With no overstory the logarithmic velocity profile is assumed to extend to the understory source height, and the resistance associated with this profile is given by

$$r_{ai} = \frac{\ln [[x - d_u]/z_{0u}]}{u(x)k^2} \ln [[x - d_u]/Z''] \tag{A5}$$

Total resistances for the overstory and understory are calculated through (A5) with $Z'' = d_o + z_{0o} - d_u$ and $Z'' = z_{0u}$, respectively. If snow covers the understory, r_{ao} and r_{as} are calculated with $d_u = z_s$ and $z_{0u} = z_{0s}$. Total resistance for the soil is given by

$$r_{ag} = r_{au} + \frac{\ln [[x - d_u]/z_{0u}]h_u e^n}{u(x)k^2(h_u - d_u)n} [\exp (-nz_n/h_u) - \exp [-n[d_u + z_{0u}]/h_u]] + r_{\log} \tag{A6}$$

with $r_{\log}$ calculated using (A1).

A2. Resistances With an Incomplete Overstory Cover

It is assumed that aerodynamic resistance varies linearly with LAI_o and F between the values associated with their

two limits, no overstory (LAI_o and/or F equal zero) and a complete overstory cover. A complete cover is defined as $F = 1$ and $LAI_o = LAI_c$. Thus with $L = FLAI_o$

$$r_{aj} = \frac{1}{LAI_c} L r_{aj}(C) + \frac{1}{LAI_c} (LAI_c - L) r_{aj}(0)$$

$$0 \le L \le LAI_c \qquad \text{(A7)}$$

$$r_{aj} = r_{aj}(C) \qquad L > LAI_c \qquad \text{(A8)}$$

where $r_{aj}(C)$ are resistances associated with a complete overstory calculated using (A1)–(A4) and $r_{aj}(0)$ are resistances assuming no overstory calculated using (A5) and (A6).

The aerodynamic resistance for snow (r_{as}) is adjusted for atmospheric stability using the method of *Choudhury and Monteith* [1988]. If the snowpack is colder than the atmosphere (stable conditions), the air near the surface is cooled, becomes denser and resists being lifted from the snowpack surface, and cannot be replaced as quickly by warmer or moist air. In unstable (lapse) conditions, vertical motion is enhanced by buoyancy. Under these conditions

stable

$$r_{as} = r_{as}/(1 + \delta)^2 \qquad \delta < 0 \qquad \text{(A9a)}$$

unstable

$$r_{as} = r_{as}/(1 + \delta)^{3/4} \qquad \delta > 0 \qquad \text{(A9b)}$$

where

$$\delta = 5g(z_n - z_s)(T_s - T_a)/((T_a + 273)u(z_n)^2)$$

where g is the gravitational acceleration.

Acknowledgments. This research was supported by a U.S. Department of Energy Global Change Distinguished Postdoctoral Fellowship to the first author, and by the Global Studies Program at Pacific Northwest Laboratory. The Global Change Distinguished Postdoctoral Fellowship is sponsored by the U.S. Department of Energy, Office of Health and Environmental Research, and administered by Oak Ridge Associated Universities. Pacific Northwest Laboratory is operated for the U.S. Department of Energy by Battelle Memorial Institute under contract DE-ACO6-76RLO 1830.

References

Abbott, M. B., J. C. Bathurst, J. A. Cunge, P. E. O'Connell, and J. Rasmussen, An introduction to the European Hydrological System–Système Hydrologique Européen, "SHE," 1, History and philosophy of a physically-based, distributed modelling system, *J. Hydrol.*, *87*, 45–59, 1986a.

Abbott, M. B., J. C. Bathurst, J. A. Cunge, P. E. O'Connell, and J. Rasmussen, An introduction to the European Hydrological System–Système Hydrologique Européen, "SHE," 2, Structure of a physically-based, distributed modelling system, *J. Hydrol.*, *87*, 61–77, 1986b.

Alexander, R. R., C. A. Troendle, M. R. Kaufmann, W. D. Shepperd, G. L. Crouch, and R. K. Watkins, The Fraser experimental forest, Colorado: Research program and published research 1937–1985, *Gen. Tech. Rep. RM-118*, 44 pp., Rocky Mt. For. and Range Exp. Stn., U.S. Dept. of Agric. For. Serv., Fort Collins, Colo., 1985.

Anderson, E. A., Development and testing of snowpack energy balance equations, *Water Resour. Res.*, *4*(1), 19–37, 1968.

Arola, A., Effects of subgrid scale spatial variability on mesoscale snow modeling, M.S. thesis, Dept. of Civ. Eng., Univ. of Washington, Seattle, 1993.

Band, L. E., D. L. Peterson, S. W. Running, J. Coughlan, R. Lammers, J. Dungan, and R. Nemani, Forest ecosystem processes at the watershed scale: Basis for distributed simulation, *Ecol. Modell.*, *56*, 171–196, 1991.

Band, L. E., P. Patterson, R. Nemani, and S. W. Running, Forest ecosystem processes at the watershed scale: Incorporating hillslope hydrology, *Agric. For. Meteorol.*, *63*, 93–126, 1993.

Barros, A. P., and D. P. Lettenmaier, Dynamic modeling of the spatial distribution of precipitation in remote mountainous areas, *Mon. Weather Rev.*, *121*, 1195–1214, 1993.

Beven, K. J., On subsurface stormflow: An analysis of response times, *Hydrol. Sci. J.*, *4*, 505–521, 1982.

Beven, K. J., and M. J. Kirkby, A physically based, variable contributing area model of basin hydrology, *Hydrol. Sci. Bull.*, *24*(1), 43–69, 1979.

Bonan, G. B., A biophysical surface energy budget analysis of soil temperature in the boreal forests of interior Alaska, *Water Resour. Res.*, *27*(5), 767–781, 1991.

Bristow, K. L., and G. S. Campbell, On the relationship between incoming solar radiation and daily maximum and minimum temperature, *Agric. For. Meteorol.*, *31*, 159–166, 1984.

Brooks, R. H., and A. T. Corey, Hydraulic properties of porous media, *Hydrol. Pap.*, *3*, Colo. State Univ., Fort Collins, 1964.

Campbell, G. S., *An Introduction to Environmental Biophysics*, 159 pp., Springer-Verlag, New York, 1977.

Choudhury, B. J., and J. L. Monteith, A four-layer model for the heat budget of homogeneous land surfaces, *Q. J. R. Meteorol. Soc.*, *114*, 373–398, 1988.

Dickinson, R. E., A. Henderson-Sellers, P. J. Kennedy, and M. F. Wilson, Biosphere-atmosphere transfer scheme (BATS) for the NCAR Community Climate Model, *Tech. Note NCAR/TN-275+STR*, Natl. Cent. for Atmos. Res., Boulder, Colo., 1986.

Dickinson, R. E., A. Henderson-Sellers, C. Rosenzweig, and P. J. Sellers, Evapotranspiration models with canopy resistance for use in climate models, A review, *Agric. For. Meteorol.*, *54*, 373–388, 1991.

Eagleson, P. S., Climate, soil, and vegetation, 3, A simplified model of soil moisture movement in the liquid phase, *Water Resour. Res.*, *14*(5), 722–730, 1978a.

Eagleson, P. S., Climate, soil, and vegetation, 4, The expected value of annual evapotranspiration, *Water Resour. Res.*, *14*(5), 731–739, 1978b.

Entekhabi, D., and P. S. Eagleson, Land surface hydrology parameterization for atmospheric general circulation models: Inclusion of subgrid scale spatial variability and screening with a simple climate model, *Rep. 325*, Ralph M. Parsons Lab., 195 pp., Mass. Inst. of Technol., Cambridge, 1989.

Famiglietti, J. S., E. F. Wood, M. Sivapalan, and D. J. Thongs, A catchment scale water balance model for FIFE, *J. Geophys. Res.*, *97*(D17), 18,997–19,007, 1992.

Feddes, R. A., P. J. Kowalik, and H. Zaradny, *Simulation of Field Water Use and Crop Yield*, 188 pp., John Wiley, New York, 1978.

Frew, J. E., The image processing Workbench, Ph.D. thesis, 382 pp., Dept. of Geogr., Univ. of Calif., Santa Barbara, 1990.

Hunt, E. R., Jr., S. W. Running, and C. A. Federer, Extrapolating plant water flow resistances and capacitances to regional scales, *Agric. For. Meteorol.*, *54*, 169–195, 1991.

Kaufmann, M. R., Leaf conductance as a function of photosynthetic photon flux density and absolute humidity difference from leaf to air, *Plant Physiol.*, *69*, 1018–1022, 1982.

Kaufmann, M. R., C. B. Edminster, and C. A. Troendle, Leaf area determinations for subalpine tree species in the central Rocky Mountains, *Res. Pap. RM-238*, 7 pp., Rocky Mt. For. and Range Exp. Stn., U.S. Dept. of Agric. For. Serv., Fort Collins, Colo., 1982.

Laramie, R. L., and J. C. Schaake, Jr., Simulation of the continuous snowmelt process, *Rep. 143*, Ralph M. Parsons Lab., Mass. Inst. of Technol., Cambridge, 1972.

Legates, D. R., and T. L. DeLiberty, Precipitation measurement biases in the United States, *Water Resour. Bull.*, *29*(5), 855–861, 1993.

Linsley, R. K., M. A. Kohler, and J. L. H. Paulhus, *Hydrology for Engineers*, 508 pp., McGraw-Hill, New York, 1982.

Longley, K., D. Jacobsen, and D. Marks, Supplement to the image

processing workbench (IPW), report, Environ. Res. Lab., U.S. Environ. Protect. Agency, Corvallis, Oreg., 1992.

Loveland, T. R., J. W. Merchant, D. O. Ohlen, and J. F. Brown, Development of a land-cover characteristics database for the conterminous U.S., *Photogramm. Eng. Remote Sens.*, *57*, 1453–1463, 1991.

Monteith, J. L., Evaporation and surface temperature, *Q. J. R. Meteorol. Soc.*, *107*, 1–27, 1981.

Monteith, J. L., and M. H. Unsworth, *Principles of Environmental Physics*, 291 pp., Routledge Chapman and Hall, New York, 1990.

Rawls, W. J., and D. L. Brakensiek, Estimation of soil water retention and hydraulic properties, in *Unsaturated Flow in Hydrologic Modeling—Theory and Practice, NATO ASI Ser. C: Math. and Phys. Sci.*, vol. 275, edited by H. J. Morel-Seytoux, pp. 275–300, Kluwer Academic, Hingham, Mass., 1989.

Running, S. W., Computer simulation of regional evapotranspiration by integrating landscape biophysical attributes with satellite data, in *Land Surface Evaporation Measurement and Parameterization*, edited by T. J. Schmugge and J. C. André, pp. 359–370, Springer-Verlag, New York, 1991.

Running, S. W., and J. C. Coughlan, A general model of forest ecosystem processes for regional applications, I. Hydrologic balance, canopy gas exchange, and primary production processes, *Ecol. Modell.*, *42*, 125–154, 1988.

Running, S. W., R. R. Nemani, and R. D. Hungerford, Extrapolation of synoptic meteorological data in mountainous terrain and its use for simulating forest evapotranspiration and photosynthesis, *Can. J. For. Res.*, *17*, 472–483, 1987.

Sellers, P. J., Y. Mintz, Y. C. Sud, and A. Dalcher, A simple biosphere model (SiB) for use within general circulation models, *J. Atmos. Sci.*, *43*(6), 505–531, 1986.

Sellers, P. J., F. G. Hall, G. Asrar, D. E. Strebel, and R. E. Murphy, An overview of the first international satellite land surface climatology project (ISLSCP) field experiment (FIFE), *J. Geophys. Res.*, *97*(D17), 18,345–18,371, 1992.

Shuttleworth, W. J., and J. S. Wallace, Evaporation from sparse crops—An energy combination theory, *Q. J. R. Meteorol. Soc.*, *111*, 839–855, 1985.

Sivapalan, M., K. Beven, and E. F. Wood, On hydrologic similarity, 2, A scaled model of storm runoff production, *Water Resour. Res.*, *23*(12), 2266–2278, 1987.

U.S. Army Corps of Engineers, Snow hydrology, Summary report of the snow investigations, N. Pac. Div., U.S. Army Corps of Eng., Portland, Oreg., 1956.

D. P. Lettenmaier, Department of Civil Engineering, FX 10, University of Washington, Seattle, WA 98195.

L. W. Vail and M. S. Wigmosta, Pacific Northwest Laboratory, P. O. Box 999, Richland, WA 99352.

(Received August 30, 1993; revised January 26, 1994; accepted February 9, 1994.)